



Cite this: *RSC Adv.*, 2020, 10, 6114

Ag₂O-decorated electrospun BiVO₄ nanofibers with enhanced photocatalytic performance†

Junpeng Ren * and Yongyong Zhu*

Semiconductor photocatalysts are emerging as tools for pollutant degradation in industrial wastewater, air purification, antibacterial applications, etc. due to their use of visible light, which is abundant in sunlight. Here, we report a new type of p–n junction Ag₂O/BiVO₄ heterogeneous nanostructured photocatalyst with enhanced photocatalytic performance. P-type Ag₂O nanoparticles were *in situ* reduced and assembled on the surface of electrospun BiVO₄ nanofibers using ultraviolet (UV) irradiation; this process hindered the recombination of localized photogenerated electron–hole pairs, and hence resulted in the enhanced photocatalytic activity of the BiVO₄/Ag₂O nanocomposites. The photocatalytic activities of the obtained BiVO₄ and BiVO₄/Ag₂O nanocomposites were assessed by measuring the degradation of rhodamine B (RhB) under visible light. The 10 wt% Ag₂O/BiVO₄ sample yielded the optimum degradation of RhB (98.47%), much higher than that yielded by pure BiVO₄ nanofibers (64.67%). No obvious change in the XRD pattern of an Ag₂O/BiVO₄ sample occurred as a result of its use in the photocatalytic reaction, indicating its excellent stability. The high photocatalytic performance observed was attributed to the large surface-to-volume ratio of the essentially one-dimensional electrospun BiVO₄ nanofibers and to the *in situ* growth of p-type Ag₂O on the surface of the n-type BiVO₄ nanofibers.

Received 27th December 2019

Accepted 25th January 2020

DOI: 10.1039/c9ra10952h

rsc.li/rsc-advances

1. Introduction

Metal oxide semiconductor photocatalysts have been used to greatly alleviate such problems as water pollution and those involving the environment and energy issues by using visible light of the solar spectrum, in particular collecting it to generate charge carriers, and promoting charge separation and transfer.^{1–5} TiO₂ is an excellent photocatalyst and is also strongly oxidizing, chemically stable, inexpensive and non-toxic, and has been widely studied.^{6,7} However, the band gap of TiO₂ is approximately 3.2 eV, which leads to a rapid recombination of the photogenerated electron–hole pairs and absorption of only ultraviolet (UV) light (only about 4% of total sunlight), and hence TiO₂ is not a suitable and effective photocatalyst for water purification.^{8,9} Recently, n-type bismuth vanadate (BiVO₄) with a monoclinic scheelite-like structure has become considered as a promising class of photocatalysts owing to its narrower band gap of 2.4 eV compared to that of TiO₂, resulting in an easy separation of photogenerated electrons from holes and excellent photocatalytic performance.^{10–14}

The morphology, structure and specific surface area of BiVO₄ materials obtained *via* traditional approaches, however, have not met the requirements for more efficient photocatalysis

development.^{15,16} Nevertheless, by controlling the morphologies and structures of BiVO₄ and BiVO₄ materials modified with noble metals and its oxides, further improvements of the photocatalytic performances of BiVO₄ materials can be realized.¹⁷ With regards to the control of morphology, in comparison with decahedral BiVO₄ structures and BiVO₄ nanorods, nanobelts, nanotubes and nanospheres, one-dimensional (1D) BiVO₄ nanofibers (NFs) display many advantages: (1) large surface-to-volume ratios, which could prolong the photocarrier lifetime; (2) very large aspect ratios, forming a unique charge transfer path along the 1D direction; and (3) abundant surface active sites, which could provide many active sites for subsequent surface modifications of the BiVO₄.^{18–24} As for modifications with noble metals, doping n-type noble metals oxides onto the surfaces of p-type bismuth vanadate semiconductors is a feasible way to construct p–n heterojunctions with enhanced photocatalytic performances.^{25–28}

Based on these considerations, we prepared p–n junction Ag₂O/BiVO₄ heterogeneous structures by *in situ* reducing Ag₂O nanoparticles on the surfaces of 1D electrospun BiVO₄ NFs. As-obtained 10 wt% Ag₂O/BiVO₄ NFs showed enhanced photocatalytic activity towards degradation of rhodamine B (RhB) pollutants under visible light (photocatalytic efficiency: 98.47% within 100 minutes). Moreover, after three photodegradation cycles, the degradation efficiency was still about 90%, indicating its outstanding cycle stability. Theoretical studies indicated this enhanced photocatalysis to be due to the 1D nature of the electrospun BiVO₄ NFs and due to the construction of p–n junction Ag₂O/BiVO₄ heterogeneous structures.

College of Weapons Engineering, Naval University of Engineering, Wuhan, 430033 China. E-mail: 693301875@qq.com; zyy99515@126.com

† Electronic supplementary information (ESI) available. See DOI: 10.1039/c9ra10952h



2. Experimental

2.1. Synthesis of BiVO₄ NFs

BiVO₄ NFs were synthesized by employing the electrospinning method. In a typical process, 1.21 g of Bi(NO₃)₃·5H₂O and 0.662 g of vanadyl acetylacetonate (VO(acac)₂) were dissolved in 5 mL of *N,N*-dimethylformamide (DMF) under magnetic stirring for 2 h. Afterwards, a mass of 0.7 g of polyvinyl pyrrolidone (PVP) was added to the above mixture under magnetic stirring for 8 h to form a bottle green precursor spinning solution. This solution was drawn up into a 10 mL plastic syringe *via* a stainless steel needle with an inner diameter of 0.5 mm, and then a voltage of 18 kV was applied over a distance of 15 cm between the needle tip and an aluminium foil collector. After carrying out the collection process for 1 h, the generated precursor was dried in a vacuum oven at 60 °C for 12 h. Finally, the dried BiVO₄ precursor was calcinated in a muffle furnace set at various temperatures (400 °C, 500 °C, 600 °C) each for 1 h and with a constant heating rate of 1 °C min⁻¹ between these levels.²⁹

2.2. *In situ* growth of Ag₂O nanoparticles on the BiVO₄ NFs

Ag₂O nanoparticles were *in situ* reduced and assembled on the surfaces of BiVO₄ NFs by applying ultraviolet (UV) irradiation. First, in each of series of samples, a mass of 0.1 g of as-prepared BiVO₄ calcinated at 500 °C was dispersed in 40 mL of deionized water. To these samples were added AgNO₃ at different mass fractions, of 3%, 5%, 10% and 15%, respectively, to form suspensions under magnetic stirring. The suspensions were stirred under UV light illumination for 5 h. The final powders were washed with deionized water several times, and then dried at 60 °C in the air for 12 h.

2.3. Characterizations

The morphologies, structures and crystalline forms of BiVO₄ NFs and Ag₂O-doped BiVO₄ NFs were investigated by using a scanning electron microscope (SEM, MAGELLIAN-400), transmission electron microscope (TEM, JEM-2200FS), and X-ray powder diffractometer system (XRD, Rigaku D/max-2550), respectively. The change in the mass of a BiVO₄ precursor as a function of temperature and time was assessed by acquiring thermogravimetric analysis and differential scanning calorimetry (TGA/DSC) curves in the isothermal mode using a TA SDT Q600 thermogravimetry analyzer. Raman spectra were acquired by using a Raman spectroscopy apparatus (Spex 1403) with a 514 nm-wavelength laser to identify the molecular structures of the samples. X-ray photoelectron spectroscopy (XPS) data were measured with an ESCALAB 250 electron spectrometer to characterize the surface chemical states of the samples. An absorption spectrum was obtained with a UV-Vis spectrophotometer (UV-2450), using BaSO₄ as a reference.

3. Results and discussion

Fig. 1a and S1a† show the SEM images acquired of the BiVO₄ precursor. Inspection of the images showed a very smooth surface of the BiVO₄ precursor, attributed to it containing the high-molecular-weight PVP template. The BiVO₄ precursor formed

fibers with an average diameter of 500 nm. Fig. S1b–d† display the SEM images acquired of the BiVO₄ precursors calcinated at 400 °C, 500 °C and 600 °C. Inspection of these images showed the roughness and variation in diameter of the BiVO₄ NFs after calcination, features attributed to the volatilization of the DMF and PVP. When the temperature reached 500 °C, many pores were observed evenly distributed on the surfaces of the BiVO₄ NFs, and the average NF diameter decreased to about 250 nm. When the annealing temperature was further increased, the NFs gradually broke apart, so we chose the BiVO₄ NFs annealed at 500 °C as the template to grow Ag₂O particles. The XRD of the BiVO₄ NFs (Fig. S2†) calcinated at the three temperatures also demonstrated that the crystallinity of the NFs annealed at 500 °C was the best. The acquired SEM images of the Ag₂O/BiVO₄ NFs are shown in Fig. 1b and c. Ag₂O particles were observed to be uniformly distributed on the BiVO₄ NFs. Fig. 1d shows the acquired SEM image of a single Ag₂O/BiVO₄ NF and images of its corresponding elemental mapping. The dot mapping images of Bi, V, O, and Ag followed closely the backbone of the NF, suggesting the successful synthesis of the Ag₂O/BiVO₄ NFs. A closer TEM observation of an Ag₂O/BiVO₄ NF (Fig. 1e) indicated that the equally distributed Ag₂O particles did not change the fiber structure of BiVO₄. Fig. 1f shows a high-resolution TEM (HRTEM) image of a marginal area of the Ag₂O/BiVO₄ NF shown in Fig. 1e, and indicated the monoclinic structure of the as-synthesized BiVO₄ NFs and Ag₂O particles. The lattice constant measured from the scheelite-like structure of the BiVO₄ NF was 0.308 nm, in agreement with the (112) planes of the BiVO₄ phase.¹³ A lattice spacing value of 0.236 nm was assigned to the (200) planes of the Ag₂O phase. The selected area electron diffraction pattern (Fig. 1g) acquired from an Ag₂O/BiVO₄ NF showed the same good crystallinity and nanocomposite structure. The energy dispersive X-ray (EDX) spectrum acquired of an Ag₂O/BiVO₄ NF is shown in Fig. 1h, and revealed that the NF was composed of Bi, V, O and Ag elements. Fig. 1i shows thermogravimetric analysis and differential scanning calorimetry (TGA/DSC) curves indicative of the synthesis of porous BiVO₄ NFs.³⁰ Analysis of the acquired X-ray diffraction (XRD) pattern (Fig. 1j) further confirmed that the as-synthesized NFs were monoclinic scheelite-like-structured BiVO₄ NFs (JCPDS card no. 75-2480).^{17,31,32} None of the XRD patterns of the samples showed any characteristic diffraction peak corresponding to Ag₂O particles, attributed to the small quantities of Ag₂O in the as-synthesized samples.

XPS data were collected to monitor the elemental composition of the nanocomposites and valence states of the elements, as shown in Fig. 2. Fig. 2a shows the survey XPS spectrum of Ag₂O/BiVO₄ NFs. Analysis of this spectrum indicated that the samples consisted of Bi, V, O and Ag elements, in agreement with the results of mapping images and the EDX spectrum. The acquired high-resolution XPS spectrum of the Ag₂O/BiVO₄ NFs in the Bi 4f, V 2p, O 1s and Ag 3d regions are shown in Fig. 2b–e, respectively. In the Bi 4f region (Fig. 2b), the two peaks located at 159.35 eV and 164.67 eV can be attributed to the binding energies of Bi 4f_{5/2} and Bi 4f_{7/2} with a spin-orbit splitting energy of 5.32 eV, demonstrating that element Bi was present in the form Bi³⁺. Fig. 2c displays the V 2p region of the spectrum, which can be deconvoluted into two sets of peaks centered at 517.3 eV and 524.9 eV, corresponding to V 2p_{3/2} and V 2p_{5/2} with a spin-orbit

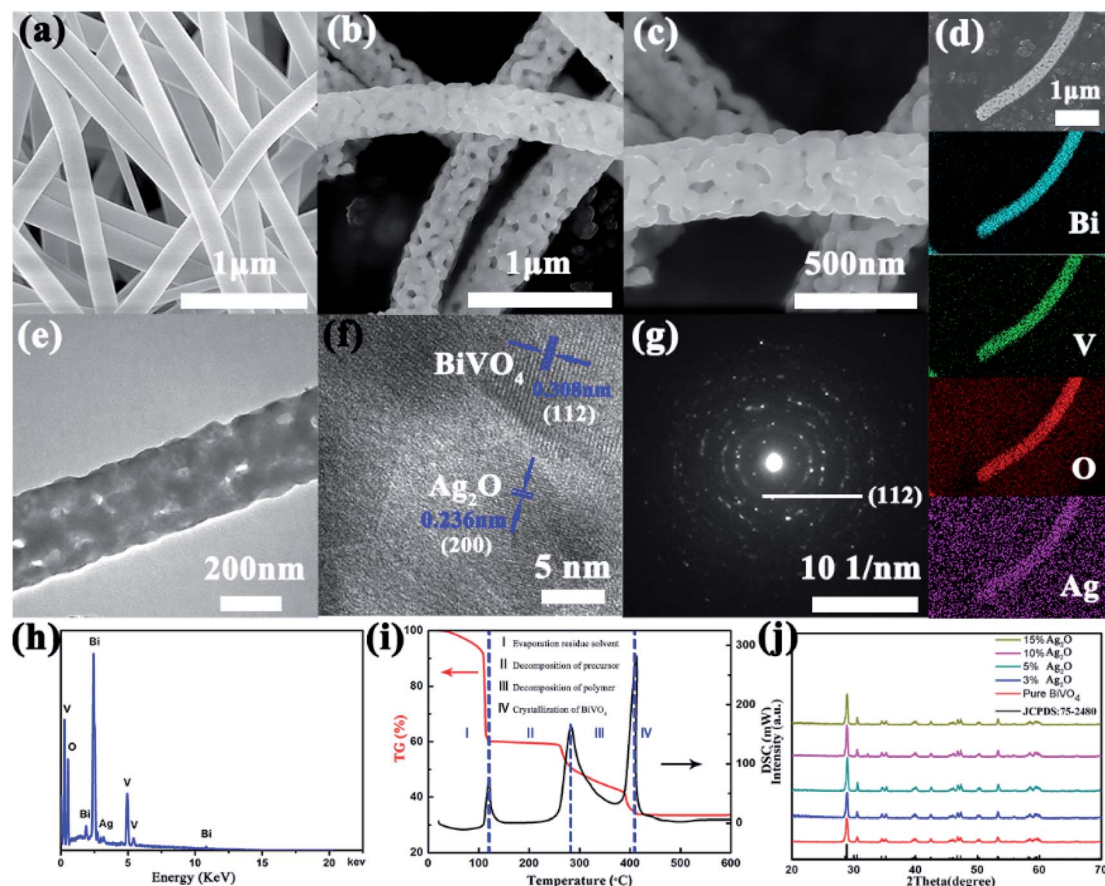


Fig. 1 (a) An SEM image of an obtained BiVO_4 precursor. (b and c) Typical SEM images of Ag_2O -doped BiVO_4 NFs. (d) An SEM image of a single $\text{Ag}_2\text{O}/\text{BiVO}_4$ NF with the corresponding Bi, V, O and Ag elemental mapping images. (e) A TEM image and (f) high-resolution TEM (HRTEM) image of an $\text{Ag}_2\text{O}/\text{BiVO}_4$ NF. (g) Selected area electron diffraction (SAED) pattern and (h) EDAX data of the $\text{Ag}_2\text{O}/\text{BiVO}_4$ NF taken from the area marked in (b). (i) TGA/DSC curves of $\text{Ag}_2\text{O}/\text{BiVO}_4$ NFs (TGA curve: red; DSC curve: black; heating range: 30–600 °C with a rate of 5 °C min⁻¹). (j) XRD patterns of pure BiVO_4 and $\text{Ag}_2\text{O}/\text{BiVO}_4$ composites.

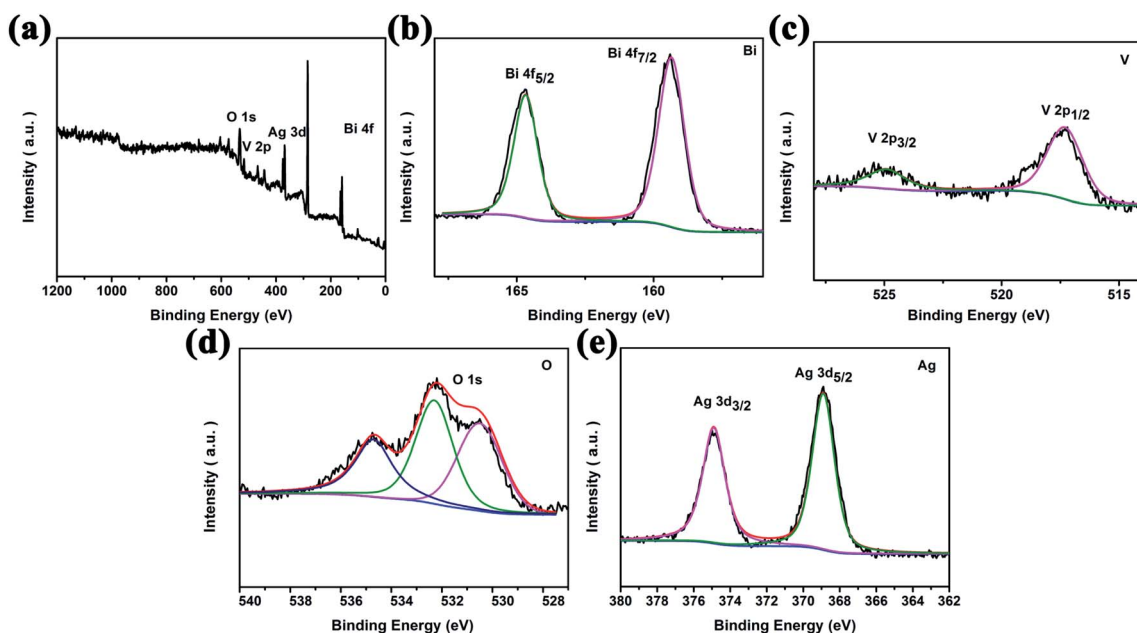


Fig. 2 High-resolution XPS spectra of 10 wt% $\text{Ag}_2\text{O}/\text{BiVO}_4$ samples: (a) the survey spectrum and (b) Bi 4f, (c) V 2p, (d) O 1s, and (e) Ag 3d spectra.



splitting energy of 7.6 eV.^{33,34} In comparison with XPS spectra of pure BiVO₄ NFs (Fig. S3†), no obvious change was found in the spin-orbit splitting energy values of the Bi and V elements, but for the O element, a new peak at 534.7 eV and attributed to Ag₂O appeared in the O 1s region of the XPS spectrum of the hybrid composites. To further determine the valence state of the elements Ag, the high-resolution XPS spectrum in its Ag 3d region (Fig. 2e) was further analyzed. Two observed peaks at 374.9 eV and 368.9 eV can be ascribed to the binding energies of Ag 3d_{3/2} and Ag 3d_{5/2} with a spin-orbit splitting energy of 6 eV, consistent with the chemical state of Ag₂O. All above analysis results taken together showed that the Ag₂O nanoparticles became tightly bound to the surfaces of the BiVO₄ NFs, beneficial for the photocatalytic performance.

After characterizing the elementary morphologies and structures of the Ag₂O/BiVO₄ NFs, photocatalytic performance studies were systematically conducted. First, UV-Vis diffuse absorption spectra (UV-Vis DRS) of as-prepared samples were acquired, as shown in Fig. 3a and S4,† to investigate their photo-absorption properties. According to the UV-Vis DRS of pure BiVO₄ shown in Fig. S4,† the sample showed relatively strong absorption of light at wavelengths of 300 to 450 nm, but weakening absorption as the wavelength of the light was increased above 450 nm, indicating that BiVO₄ by itself can only be excited by UV light. After BiVO₄ was decorated with Ag₂O nanoparticles, the UV-Vis DRS of the resulting Ag₂O/BiVO₄ NFs (Fig. 3a) showed a significant red-shift of the absorption compared to that of the pure BiVO₄ NFs. All the composites with different mass ratios exhibited enhanced absorption of visible light, which can be attributed to the heterojunction formed between Ag₂O and BiVO₄ NFs having changed the optical properties of the photocatalyst, and suggesting that it would display outstanding activity in the visible light region. The p-n heterojunction effectively decreased the coupling of the photogenerated electron-hole pairs, thus resulting in the enhanced visible light absorption. The corresponding photocurrent density was measured in a three-electrode system in a 0.5 M K₂SO₄ aqueous electrolyte with a Pt counter electrode, an Ag/AgCl reference electrode, and as-prepared Ag₂O/BiVO₄ NFs serving as the working electrode. The

photocurrent-time curves of Ag₂O/BiVO₄ NFs with various mass ratios are displayed in Fig. 3b. These curves showed that the photocurrent density of the 10% Ag₂O/BiVO₄ NFs was greater than that of the samples with other proportions of the components and with the same illumination time. This result can be attributed to n-type Ag₂O in moderate amounts being able to hinder photonic electron-hole pairs from recombining and excess Ag₂O nanoparticles in the nanocomposites forming a load center of carriers and hence impeding the separation of photogenerated electrons and holes.

Fig. 4a shows the degradation of an RhB pollutant under visible light irradiation using pure BiVO₄ NFs as well as Ag₂O/BiVO₄ samples with various mass ratios. No obvious degradation was observed in the absence of any photocatalyst. When any of the as-prepared Ag₂O/BiVO₄ photocatalysts were added, the RhB pollutant almost fully degraded after irradiation of 100 min. In the presence of pure BiVO₄, 3%, 5%, 10%, and 15% Ag₂O/BiVO₄, 64.67%, 90.2%, 96.65%, 98.47%, and 96.65%, respectively, of the initial amount of RhB degraded within the 100 minutes. The 10% Ag₂O/BiVO₄ NFs exhibited the highest activity, with the degradation rate increased by 32.8% compared to that of the pure BiVO₄ NFs. The kinetic curves of RhB degradation are displayed in Fig. 4b, and indicated that the degradation can be approximated as a pseudo-first-order process following the linear transform $\ln(C_0/C_t) = kt$, where k is the degradation rate constant.^{35,36} All of the Ag₂O/BiVO₄ composites exhibited higher photocatalytic activities than did the bare BiVO₄. The degradation rate constant (k) of the Ag₂O/BiVO₄ with a 10% mass ratio was calculated to be 0.03908 min⁻¹, a value quite remarkably about 1.62, 1.23 and 1.96 times those for the Ag₂O/BiVO₄ samples with 3%, 5% and 15% Ag₂O loads, respectively. The above two results indicated that decoration of Ag₂O nanoparticles on the surface of BiVO₄ NFs did indeed improve the photocatalytic properties, and indicated that using the appropriate mass ratio of Ag₂O in the as-prepared composites was crucial to the synergistic effects during the photocatalytic reaction. Therefore, we chose 10% of Ag₂O/BiVO₄ for further study. To investigate the effect of photocatalyst dosage on the photocatalytic performances, photocatalytic reductions of RhB using various masses of 10% Ag₂O/

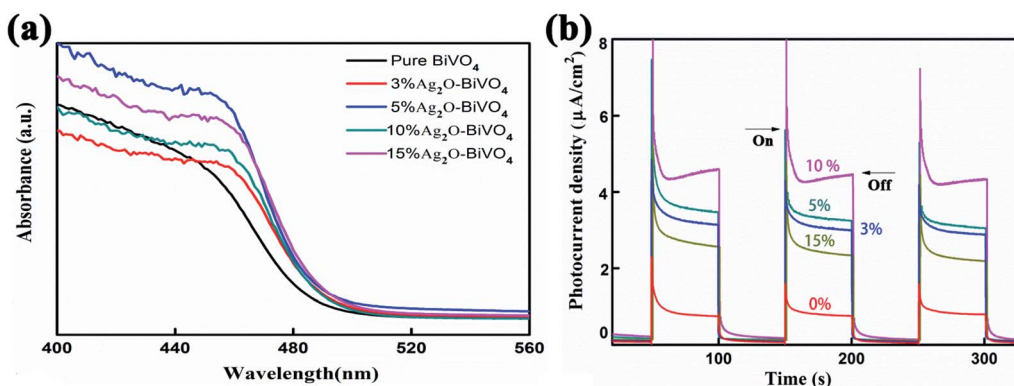


Fig. 3 (a) UV-Vis diffuse absorption spectra of pure BiVO₄ photocatalysts and Ag₂O/BiVO₄ samples with various mass ratios of the components. (b) The corresponding photocurrent density curves.

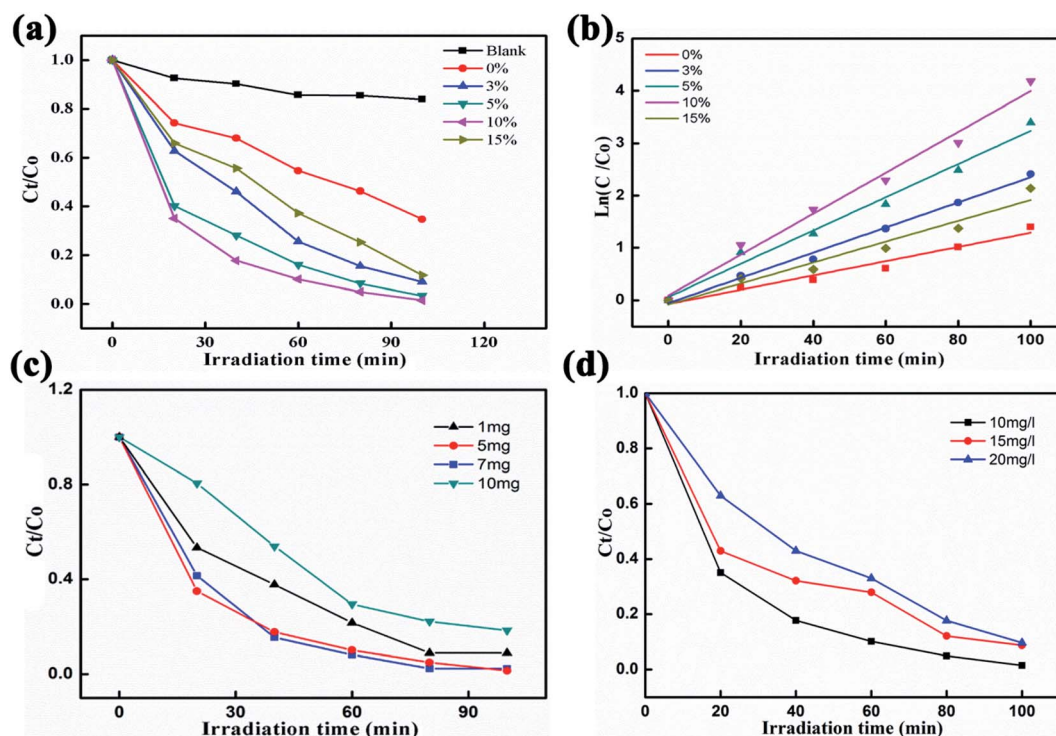


Fig. 4 (a) Photocatalytic reductions of RhB using pure BiVO_4 photocatalysts and $\text{Ag}_2\text{O}/\text{BiVO}_4$ samples with various mass ratios. (b) The linear relationships of $\ln(C/C_0)$ versus time for the degradation of RhB. (c) Photocatalytic reductions of RhB in the presence of various masses of 10 wt% $\text{Ag}_2\text{O}/\text{BiVO}_4$ photocatalyst under visible-light irradiation. (d) Photocatalytic reductions of various concentrations of RhB using 10 wt% $\text{Ag}_2\text{O}/\text{BiVO}_4$.

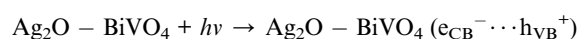
BiVO_4 photocatalysts under visible-light irradiation were performed, as shown in Fig. 4c. Notably, a mass of 5 mg of the $\text{Ag}_2\text{O}/\text{BiVO}_4$ photocatalyst degraded nearly all of the RhB pollutant. In contrast, when using more of the photocatalyst, the photocatalytic performance was poorer. This result was attributed to excessive photocatalyst in the RhB solution increasing the turbidity of the solution, a feature adverse to the penetration of visible light. The photocatalytic reductions of various concentrations of RhB using 5 mg of the $\text{Ag}_2\text{O}/\text{BiVO}_4$ (10%) are shown in Fig. 4d. When the initial concentration of the RhB solution was 20 mg L^{-1} , the degradation efficiency of the $\text{Ag}_2\text{O}/\text{BiVO}_4$ sample was about 10% lower than that for 10 mg L^{-1} . This result may have been due to the more concentrated solutions having been darker and hence showing worse transmittance of light, with fewer photons arriving at the surface of photocatalyst and leading to the decrease of the degradation efficiency. In addition, with the increase of the initial concentration of the solution, the surface of the photocatalyst would have produced more reactants, decreasing the density of available active sites on the surface of the photocatalyst, and hence affecting the utilization of visible light and causing the decline of the degradation efficiency.³⁷

To assess the practical applicability of the photocatalyst, the cycling stability of the 10% $\text{Ag}_2\text{O}/\text{BiVO}_4$ hybrid composite was also assessed, as shown in Fig. 5a. Even after three photocatalytic reduction processes, 90% of initial value was observed for the $\text{Ag}_2\text{O}/\text{BiVO}_4$ photocatalyst, demonstrating its

outstanding cycle performances. Fig. 5b displays the acquired XRD spectra of the $\text{Ag}_2\text{O}/\text{BiVO}_4$ photocatalyst before and after the photocatalytic reaction. We found that the phase structure of $\text{Ag}_2\text{O}/\text{BiVO}_4$ after the photodegradation was nearly the same as that before the photodegradation, showing the excellent stability and reusability of the photocatalyst.

In order to arrive at a best possible understanding of the mechanism of the photocatalysis of a heterostructured photocatalyst system, we produced a schematic of the energy diagram and charge separation in the $\text{Ag}_2\text{O}/\text{BiVO}_4$ NFs under visible light irradiation (Fig. 6). BiVO_4 and Ag_2O are n-type and p-type semiconductors, respectively, and the combination of them can form a p-n heterostructure semiconductor. Under visible-light irradiation, Ag_2O can be excited because of its relatively narrow bandgap of 1.3 eV, and the resulting photo-induced electrons would be expected to be able to transfer from the conduction band (CB) of Ag_2O to that of BiVO_4 NFs. But considering the higher CB potential of BiVO_4 NFs than those of $\text{O}_2/\text{O}_2^{\cdot-}$ (-0.33 eV) and $\text{O}_2/\text{H}_2\text{O}_2$ (0.695 eV), the electrons on the CB of BiVO_4 NFs cannot reduce O_2 to generate $\text{O}_2^{\cdot-}$, H_2O_2 , and $\cdot\text{OH}$, which are strong oxidizing groups that, if present, can break down the target RhB into H_2O , CO_2 , and so on, so as to assist in reaching the goal of improved photocatalytic performance.^{34,38–40}

The possible reactions for the degradation of RhB are as follows.



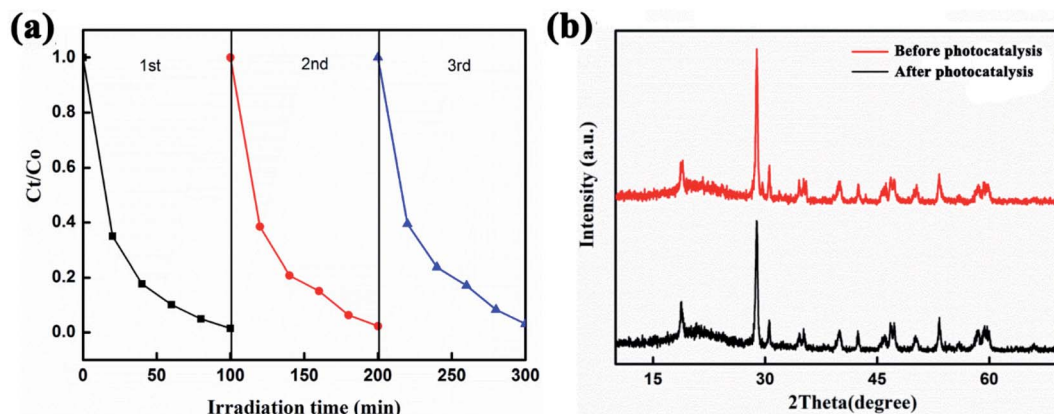
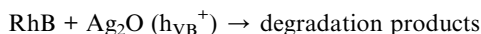
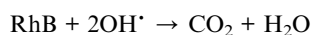
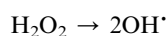
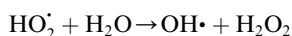
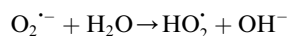
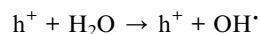
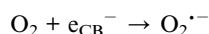
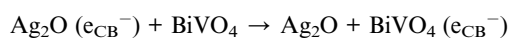


Fig. 5 (a) Three cycles of photocatalytic reductions of RhB using 10 wt% $\text{Ag}_2\text{O}/\text{BiVO}_4$ as the photocatalyst. (b) XRD patterns of $\text{Ag}_2\text{O}/\text{BiVO}_4$ before and after photocatalysis.



Here, e_{CB}^- and h_{VB}^+ denote an electron in the CB and hole in the VB, respectively.

4. Conclusions

In conclusion, a novel p-n junction $\text{Ag}_2\text{O}/\text{BiVO}_4$ heterogeneous photocatalyst has been successfully synthesized by reducing Ag_2O nanoparticles *in situ* on the surfaces of 1D electrospun BiVO_4 NFs. The obtained $\text{Ag}_2\text{O}/\text{BiVO}_4$ NFs with 10% mass ratio of Ag_2O showed 98.47% photocatalytic efficiency within 100 minutes of exposure to visible light, and showed robust cycling stability, with a degradation efficiency of 90% after three cycles. The enhanced photocatalytic performance of the $\text{Ag}_2\text{O}/\text{BiVO}_4$ heterogeneous photocatalyst can be attributed to the special 1D structure of the hybrid composites—and to the synergistic effect of Ag_2O nanoparticles and BiVO_4 NFs forming heterogeneous p-n junction structures and hence impeding the recombination of photogenerated electron-hole pairs.

Conflicts of interest

There are no conflicts to declare.

Acknowledgements

The authors sincerely acknowledge financial support from the China Postdoctoral Science Foundation (2014M550392), and a Special Financial Grant from the China Postdoctoral Science Foundation (2017T100799).

References

- 1 P. Dumrongrojthanath, T. Thongtem, A. Phuruangrat and S. Thongtem, *Superlattices Microstruct.*, 2013, **64**, 196–203.
- 2 R. V. Gonçalves, P. Migowski, H. Wender, D. Eberhardt, D. E. Weibel, F. C. Sonaglio, M. J. M. Zapata, J. Dupont, A. F. Feil and S. R. Teixeira, *J. Phys. Chem. C*, 2012, **116**, 14022–14030.

Fig. 6 A schematic illustration of the mechanism by which the p-n junctions of the $\text{Ag}_2\text{O}/\text{BiVO}_4$ samples are formed.



- 3 G. Longo, F. Fresno, S. Gross and U. L. Stangar, *Environ. Sci. Pollut. Res. Int.*, 2014, **21**, 11189–11197.
- 4 K. H. Kim and S. K. Ihm, *J. Hazard. Mater.*, 2011, **186**, 16–34.
- 5 W. Dong, D. Wang, H. Wang, M. Li, F. Chen, F. Jia and H. Li, *J. Colloid Interface Sci.*, 2019, **535**, 444–457.
- 6 W. Zhou, W. Li, J. Q. Wang, Y. Qu, Y. Yang, Y. Xie, K. Zhang, L. Wang, H. Fu and D. Zhao, *J. Am. Chem. Soc.*, 2014, **136**, 9280–9283.
- 7 C.-J. Li, J.-N. Wang, B. Wang, J. R. Gong and Z. Lin, *Mater. Res. Bull.*, 2012, **47**, 333–337.
- 8 W. Wang, L. Jing, Y. Qu, Y. Luan, H. Fu and Y. Xiao, *J. Hazard. Mater.*, 2012, **243**, 169–178.
- 9 S. S. Lee, H. Bai, Z. Liu and D. D. Sun, *Int. J. Hydrogen Energy*, 2012, **37**, 10575–10584.
- 10 F. Chen, C. Wu, J. Wang, C. P. François-Xavier and T. Wintgens, *Appl. Catal., B*, 2019, **250**, 31–41.
- 11 H. Fan, T. Jiang, H. Li, D. Wang, L. Wang, J. Zhai, D. He, P. Wang and T. Xie, *J. Phys. Chem. C*, 2012, **116**, 2425–2430.
- 12 C. Hu, J. Xu, Y. Zhu, A. Chen, Z. Bian and H. Wang, *Environ. Sci. Pollut. Res. Int.*, 2016, **23**, 18421–18428.
- 13 H. Liu, H. Hou, F. Gao, X. Yao and W. Yang, *ACS Appl. Mater. Interfaces*, 2016, **8**, 1929–1936.
- 14 B. Wang, P. Li, C. Du, Y. Wang, D. Gao, S. Li, L. Zhang and F. Wen, *RSC Adv.*, 2019, **9**, 41977–41983.
- 15 C. Regmi, Y. K. Kshetri, T.-H. Kim, R. P. Pandey and S. W. Lee, *Mol. Catal.*, 2017, **432**, 220–231.
- 16 M. J. Nalbandian, M. Zhang, J. Sanchez, Y.-H. Choa, D. M. Cwiertny and N. V. Myung, *J. Mol. Catal. A: Chem.*, 2015, **404–405**, 18–26.
- 17 H. Liu, W. Yang, L. Wang, H. Hou and F. Gao, *CrystEngComm*, 2017, **19**, 6252–6258.
- 18 J. Low, J. Yu, M. Jaroniec, S. Wageh and A. A. Al-Ghamdi, *Adv. Mater.*, 2017, **29**, 1601694.
- 19 Z. Lou and G. Shen, *Adv. Sci.*, 2016, **3**, 1500287.
- 20 S. Cavaliere, S. Subianto, I. Savych, D. J. Jones and J. Rozière, *Energy Environ. Sci.*, 2011, **4**, 4761.
- 21 D. Hou, W. Luo, Y. Huang, J. C. Yu and X. Hu, *Nanoscale*, 2013, **5**, 2028–2035.
- 22 Y. Liu, M. Zhang, L. Li and X. Zhang, *Appl. Catal., B*, 2014, **160–161**, 757–766.
- 23 H. Lu, Q. Wang, G. Li, Y. Qiu and Q. Wei, *Mater. Sci. Eng., C*, 2017, **74**, 86–93.
- 24 H. Lian and Z. Meng, *Mater. Sci. Eng., C*, 2017, **74**, 117–123.
- 25 S. Xu, D. Fu, K. Song, L. Wang, Z. Yang, W. Yang and H. Hou, *Chem. Eng. J.*, 2018, **349**, 368–375.
- 26 M. Yan, Y. Hua, F. Zhu, W. Gu, J. Jiang, H. Shen and W. Shi, *Appl. Catal., B*, 2017, **202**, 518–527.
- 27 Y. Zhao, H. Fan, K. Fu, L. Ma, M. Li and J. Fang, *Int. J. Hydrogen Energy*, 2016, **41**, 16913–16926.
- 28 Y. Zhang, G. Zhu, M. Hojamberdiev, J. Gao, J. Hao, J. Zhou and P. Liu, *Appl. Surf. Sci.*, 2016, **371**, 231–241.
- 29 K. R. Yoon, J. W. Ko, D.-Y. Youn, C. B. Park and I.-D. Kim, *Green Chem.*, 2016, **18**, 944–950.
- 30 Z. Liu, Q. Lu, C. Wang, J. Liu and G. Liu, *J. Alloys Compd.*, 2015, **651**, 29–33.
- 31 D. P. Jaihindh and Y.-P. Fu, *Catal. Today*, 2017, **297**, 246–254.
- 32 C. Liu, Y. Yang, J. Li, S. Chen, W. Li and X. Tang, *Chem. Eng. J.*, 2017, **326**, 603–611.
- 33 M. Wang, C. Niu, Q. Liu, Y. Che and J. Liu, *Mater. Sci. Semicond. Process.*, 2014, **25**, 271–278.
- 34 J. Cheng, X. Yan, Q. Mo, B. Liu, J. Wang, X. Yang and L. Li, *Ceram. Int.*, 2017, **43**, 301–307.
- 35 R. Hao, G. Wang, H. Tang, L. Sun, C. Xu and D. Han, *Appl. Catal., B*, 2016, **187**, 47–58.
- 36 J.-Q. Li, Z.-Y. Guo, H. Liu, J. Du and Z.-F. Zhu, *J. Alloys Compd.*, 2013, **581**, 40–45.
- 37 Y. Li, R. Jin, X. Fang, Y. Yang, M. Yang, X. Liu, Y. Xing and S. Song, *J. Hazard. Mater.*, 2016, **313**, 219–228.
- 38 S. Balachandran and M. Swaminathan, *J. Phys. Chem. C*, 2012, **116**, 26306–26312.
- 39 D. Wang, F. Jia, H. Wang, F. Chen, Y. Fang, W. Dong and X. Yuan, *J. Colloid Interface Sci.*, 2018, **519**, 273–284.
- 40 J. Safaei, H. Ullah, N. A. Mohamed, M. F. Mohamad Noh, M. F. Soh, A. A. Tahir, N. Ahmad Ludin, M. A. Ibrahim, W. N. R. Wan Isahak and M. A. Mat Teridi, *Appl. Catal., B*, 2018, **234**, 296–310.

